SENSORIMOTOR CONVERGENCE IN VISUAL NAVIGATION AND FLIGHT CONTROL SYSTEMS [1]

J. Sean Humbert[†]
Richard M. Murray and Michael H. Dickinson

California Institute of Technology, Pasadena, CA 91125
[†]Corresponding Author: jshumber@cds.caltech.edu

Abstract: Insects exhibit unparalleled and incredibly robust flight dynamics in the face of uncertainties. A fundamental principle contributing to this amazing behavior is rapid processing and convergence of visual sensory information to flight motor commands via spatial wide-field integration, accomplished by motion pattern sensitive interneurons in the lobula plate portion of the visual ganglia. Within a control-theoretic framework, a model for wide-field integration of retinal image flow is developed, establishing the connection between image flow kernels (retinal motion pattern sensitivities) and the feedback terms they represent. It is demonstrated that the proposed output feedback methodology is sufficient to give rise to experimentally observed navigational heuristics as the centering and forward speed regulation responses exhibited by honeybees.

Keywords: Flight Control, Navigation Systems, Output Feedback, Control Oriented Models, Autonomous Mobile Robots.

1. INTRODUCTION

Prevalent in many natural sensory systems is the phenomenon of sensorimotor convergence, wherein signals from arrays of spatially distributed and differentially tuned sensors converge in vast number onto motor neurons responsible for controlling locomotive behavior. A prime example occurs in the processing of retinal image pattern movement (optic flow) by the visuomotor systems of insects. Insect visual systems encode optic flow by combining motion estimates from arrays of local motion detectors in a way that preserves the spatial layout of the retina (Egelhaaf and Borst, 1993). This sensory information is parsed by wide-field motion sensitive interneurons (tangential cells, or LPTCs) in the lobula plate section of the visual ganglia, as shown in (Figure 1A). The output of these neurons synapse in the motor control centers, creating a sensory processing stage which spatially integrates the optic flow (Borst and Haag, 2002). This visuomotor convergence technique, spatial wide-field integration, is used by insects to extract behaviorally-relevant information from optic flow patterns to modulate the kinematics of flight (Frye and Dickinson, 2001).

Since optic flow was first recognized as a critical source of information (Gibson, 1950), there has been considerable interest in adapting this type of sensory system for bio-inspired autonomous navigation. Efforts have focused on utilizing one or more properties of optic flow to provide navigational cues (Barrows *et al.*, 2003). Examples include corridor navigation based on balancing average lateral image velocities on wheeled robots, obstacle avoidance via saccading away from regions

[1] Partial support provided by AFOSR under grant F30602-01-2-0558 and ARO under DAAD19-03-D-0004

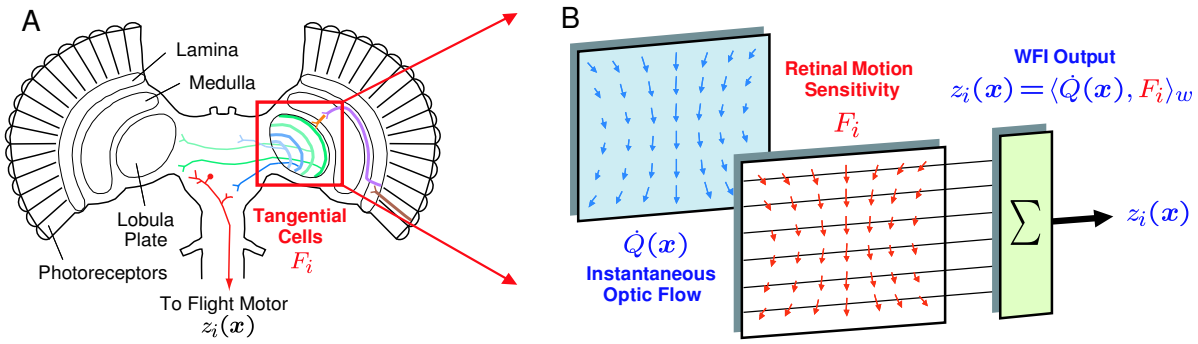

Fig. 1. (A) Visuomotor system of insects. Wide-field retinal motion sensitive interneurons (tangential cells) parse spatially-preserved visual information and transmit it to motor control centers. (B) WFI processing model. Spatial modes of optic flow are extracted by retinal motion sensitivity kernels.

with high image velocities, and optic flow based estimates of depth (Franz and Mallot, 2000). In a more traditional approach, LPTC-based processing models have been investigated as estimators for vehicle kinematic states directly from observed optic flow (Franz *et al.*, 2004), as tangential cell sensitivity maps show similarities to flow fields that correspond to egomotion (Krapp *et al.*, 1998).

In this paper we propose a more general functional role for wide-field sensitive neurons in navigation and flight control as well as a novel methodology for utilizing optic flow sensory information in bio-inspired applications. We show how the spatial harmonics of planar optic flow, extracted with motion-pattern sensitive kernels representing LPTCs (Figure 1B), correspond to feedback terms which can be used to stabilize the different navigational modes of flight. A model for wide-field integration of retinal image flow is presented in Section 2, and stabilization of obstacle avoidance and speed regulation behaviors for planar hovercraft dynamics is demonstrated in Section 3.

2. A MODEL FOR WIDE-FIELD INTEGRATION PROCESSING OF IDEAL PLANAR OPTIC FLOW

In the idealized case, optic flow is dependent on rigid body motion (translation and rotation) and on the spatial structure and distribution of objects in the environment. (Koenderink and van Doorn, 1997) provide a thorough derivation of the equations of ideal optic flow based on a three dimensional environment composed of a finite number of rigid fiducial points. In this paper we will consider the planar motion case, restricting the rigid body motion to three degrees of freedom (planar translation with single axis rotation). For analysis purposes we will consider the the optic flow to be a function of a continuous angular coordinate γ relative to the body-fixed frame b (Figure 2). Under these assumptions, the instantaneous optic flow on a circular-shaped sensor becomes a 2π-periodic function on the circle S^1 in the angular coordinate γ:

$$\dot{Q}(\gamma, \boldsymbol{x}) = -\dot{\theta} + \mu(\gamma, \boldsymbol{x}) \left(\dot{x}_b \sin\gamma - \dot{y}_b \cos\gamma \right), \quad (1)$$

where $\boldsymbol{x} = [x \;\; y \;\; \theta \;\; \dot{x}_b \;\; \dot{y}_b \;\; \dot{\theta}]'$ are the kinematics of the body-fixed frame b, and the *nearness* $\mu(\gamma, \boldsymbol{x}) = 1/r(\gamma, \boldsymbol{x})$, where $r(\gamma, \boldsymbol{x}) : [0, 2\pi] \mapsto (0, \infty)$ is the distance to the nearest obstacle along direction $\boldsymbol{Q}(\gamma) \in S^1$, restricting contact (Figure 2A). The kinematics are assumed to be

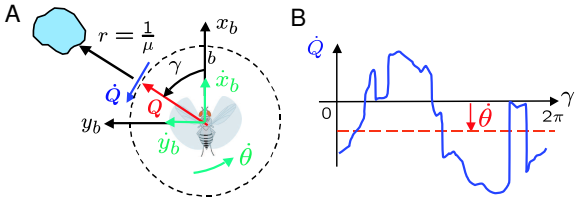

Fig. 2. (A) Body-coordinate definitions (B) Example planar optic flow

bounded functions of time, however the spatial structure of the landscape can lead to discontinuities, especially in a cluttered object field. Hence $\mu(\gamma, \boldsymbol{x})$ and $\dot{Q}(\gamma, \boldsymbol{x})$ can be considered bounded, piecewise-continuous functions of γ with a finite (countable) number of discontinuities (Figure 2B), effectively restricting them to the space of square-integrable functions $L_2[0, 2\pi] = \left\{ f : [0, 2\pi] \to \mathbb{R} : \int_0^{2\pi} |f(\gamma)|^2 \, d\gamma < \infty \right\}$.

For this treatment we will represent lobula plate tangential cells (or ipsi- and contralateral pairs as may be appropriate) by a weight $F_i(\gamma) \in L_2[0, 2\pi]$, which models their sensitivity to various retinal motion patterns. Weights $F_i(\gamma)$ are essentially a spatially distributed set static gains which are applied to the output at the corresponding local motion detectors at retinal positions γ. Through appropriate choices of $F_i(\gamma)$, we are interested in characterizing the available information relevant for use in closed loop feedback. We expect these weighting functions to be piecewise

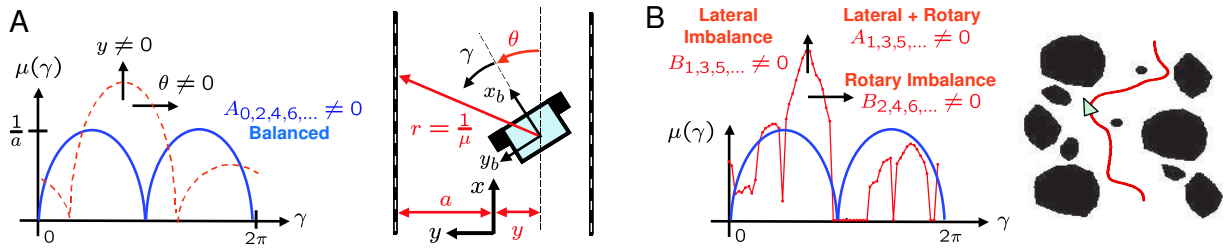

Fig. 3. Connections between WFI outputs and μ. (A) Planar tunnel geometry and lateral/rotational perturbations of μ (B) μ-shaping in environments with higher order spatial structure

continuous and square-integrable, hence the restriction to the function space $L_2[0, 2\pi]$. For this initial analysis we will also assume that optic flow estimation processing (photoreceptors and local motion detectors) have negligible dynamics, that is wide-field spatial integration (henceforth WFI) can be modeled in entirety by the transformation W, representing a spatial integration against the optic flow kernel $\dot{Q}(\gamma, \boldsymbol{x})$, which acts on elements $F_i(\gamma)$ to produce a sensor output signal z_i, hence $W : F_i \in L_2[0, 2\pi] \mapsto z_i \in \mathbb{R}$. The transformation W defined by $z_i = WF_i$ can be represented as a linear functional using the inner product structure available on $L_2[0, 2\pi]$:

$$z_i = \langle \dot{Q}, F_i \rangle_w = \frac{1}{\pi} \int_0^{2\pi} \dot{Q}(\gamma, \boldsymbol{x}) \cdot F_i(\gamma)\, d\gamma. \quad (2)$$

The inner product (2) has been defined with a factor of $1/\pi$ to be compatible with the typical Fourier harmonic component definition so that later notation is simplified.

2.1 Characterization and Interpretation of WFI Sensory Outputs for Planar Optic Flow

We are interested in characterizing the set of all possible sensory outputs available within this model and their dependency on vehicle motion and spatial distribution of objects in the environment. Since $L_2[0, 2\pi]$ is a Hilbert space, and more specifically a complete, separable inner product space, a countably infinite orthonormal basis $\{\phi_n(\gamma)\}$ exists. For fixed t, $\dot{Q}(\gamma, \boldsymbol{x}) \in L_2[0, 2\pi]$, therefore we can expand it in a generalized Fourier series $\dot{Q}(\gamma, \boldsymbol{x}) = \sum_n^\infty \langle \dot{Q}(\gamma, \boldsymbol{x}), \phi_n(\gamma) \rangle \ \phi_n(\gamma)$. If we use trigonometric Fourier series, the orthonormal basis under the inner product (2) is $\Phi = \{1/\sqrt{2}\} \cup \{\cos n\gamma : n = 1, 2, \ldots\} \cup \{\sin n\gamma : n = 1, 2, \ldots\}$, and the expansion becomes $\dot{Q}(\gamma, \boldsymbol{x}) = \frac{a_0(\boldsymbol{x})}{2} + \sum_{n=1}^\infty a_n(\boldsymbol{x}) \cos n\gamma + b_n(\boldsymbol{x}) \sin n\gamma$, where the state and nearness dependent spatial harmonics of the optic flow are defined as $a_0(\boldsymbol{x}) = \langle \dot{Q}, 1/\sqrt{2} \rangle_w = \frac{1}{\pi} \int_0^{2\pi} \dot{Q}(\gamma, \boldsymbol{x})/\sqrt{2} \ d\gamma$, $a_n(\boldsymbol{x}) = \langle \dot{Q}, \cos n\gamma \rangle_w = \frac{1}{\pi} \int_0^{2\pi} \dot{Q}(\gamma, \boldsymbol{x}) \cos n\gamma \ d\gamma$, and $b_n(\boldsymbol{x}) = \langle \dot{Q}, \sin n\gamma \rangle_w = \frac{1}{\pi} \int_0^{2\pi} \dot{Q}(\gamma, \boldsymbol{x}) \sin n\gamma d\gamma$. With some manipulations, we can rewrite these expressions in terms of the vehicle motion $(\dot{x}_b, \dot{y}_b, \dot{\theta})$ and the spatial harmonics $\{A_0, A_k, B_k : k = 1, 2, \ldots\}$ of the nearness function $\mu(\gamma, \boldsymbol{x})$:

$$\begin{aligned} a_0(\boldsymbol{x}) &= (-2\dot{\theta} + \dot{x}_b B_1 - \dot{y}_b A_1)/\sqrt{2} \quad (3) \\ a_n(\boldsymbol{x}) &= \frac{\dot{x}_b}{2} (-B_{n-1} + B_{n+1}) - \frac{\dot{y}_b}{2} (A_{n-1} + A_{n+1}) \\ b_n(\boldsymbol{x}) &= \frac{\dot{x}_b}{2} (A_{n-1} - A_{n+1}) - \frac{\dot{y}_b}{2} (B_{n-1} + B_{n+1}), \end{aligned}$$

where $\mu(\gamma, \boldsymbol{x}) = \frac{A_0(\boldsymbol{x})}{2} + \sum_{k=1}^\infty A_k(\boldsymbol{x}) \cos n\gamma + B_k(\boldsymbol{x}) \sin n\gamma$. Now, under the interpretation $W\Phi = \{a_0(\boldsymbol{x})\} \cup \{a_n(\boldsymbol{x}) : n = 1, 2, \ldots\} \cup \{b_n(\boldsymbol{x}) : n = 1, 2, \ldots\}$, the equations (3) define the action of the linear transformation $W : L_2[0, 2\pi] \mapsto \mathbb{R}$ on a basis Φ for the domain, and as such uniquely characterize the set of all possible wide-field integration sensory outputs.

The relationships in (3) define how WFI outputs depend on vehicle motion and object nearness, however, the insight required to utilize them in closed loop feedback is not readily apparent. As a motivational example, we consider a planar tunnel geometry (Figure 3A), which provides a reasonable approximation to flight between two obstacles. In this case the nearness function $\mu(\gamma, \boldsymbol{x})$ can be expressed in closed form as a function of the lateral position y, body frame orientation θ, and the tunnel half-width a:

$$\mu(\gamma, \boldsymbol{x}) = \begin{cases} \dfrac{\sin(\gamma + \theta)}{a - y} & 0 \leq \gamma + \theta < \pi \\ -\dfrac{\sin(\gamma + \theta)}{a + y} & \pi \leq \gamma + \theta < 2\pi \end{cases}. \quad (4)$$

For a centered vehicle $(y, \theta) = (0, 0)$, (4) reduces to $|\sin\gamma|/a$, which has a Fourier series expansion

$$\frac{|\sin\gamma|}{a} = \frac{2}{a\pi} - \sum_{k=2,4,6,\ldots}^\infty \frac{4}{a\pi(k^2 - 1)} \cos k\gamma. \quad (5)$$

Note that the expansion is composed of a DC component and even cosine harmonics $\{A_k : k = 0, 2, 4, \ldots\}$. (5) represents the *balanced* or *equilibrium* nearness shape (Figure 3A), as it corresponds to a position and orientation along the centerline of the tunnel. For lateral and rotary

Table 1. Planar Tunnel Spatial Fourier Decomposition

Mode	Balanced	Perturbed	Linearized
A_0	$\frac{2}{\pi a}$	$\frac{2a}{\pi(a^2-y^2)}$	$\frac{2}{\pi a}$
A_1	0	$\frac{y\sin\theta}{(a^2-y^2)}$	0
B_1	0	$\frac{y\cos\theta}{(a^2-y^2)}$	$\frac{y}{a^2}$
$A_{2,4,\ldots}$	$-\frac{4}{\pi a(k^2-1)}$	$-\frac{4a\cos k\theta}{\pi(a^2-y^2)(k^2-1)}$	$-\frac{4}{\pi a(k^2-1)}$
$B_{2,4,\ldots}$	0	$-\frac{4a\sin k\theta}{\pi(a^2-y^2)(k^2-1)}$	$-\frac{4k\theta}{\pi a(k^2-1)}$
$A_{3,5,\ldots}$	0	0	0
$B_{3,5,\ldots}$	0	0	0

displacements, the spatial harmonics of the perturbed nearness function are computed in Table 1. From the linearizations about the point $(y,\theta) = (0,0)$ it is clear that the B_1 harmonic provides an estimate of the lateral displacement while the B_2 harmonic provides an estimate of the rotary displacement. These results can be generalized to environments with more complicated spatial structure (Figure 3); nonzero $B_{1,3,5,\ldots}$ correspond to a lateral imbalance, $B_{2,4,6,\ldots}$ to a rotary imbalance, and $A_{1,3,5,\ldots}$ are coupling terms for a lateral plus a rotary imbalance.

3. WFI OUTPUT FEEDBACK

In this section we demonstrate the utility of WFI sensory outputs (3) through coupling with planar flight dynamics via static output feedback (Figure 4). The WFI operator is used to decompose the

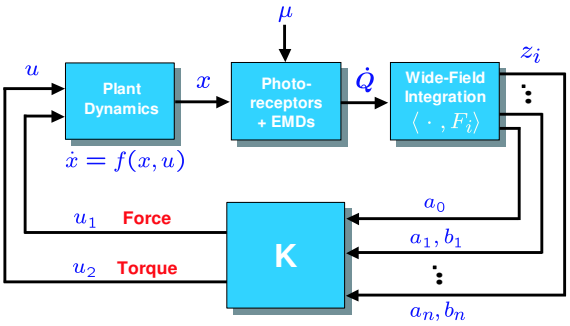

Fig. 4. Closed loop WFI output feedback

optic flow into spatial harmonics (3), and force and torque control inputs u_1, u_2 are computed as static combinations

$$u_i = K^a_{i0}\, a_0 + \sum_{j=1}^{n} K^a_{ij}\, a_j + K^b_{ij}\, b_j,$$

which correspond to motion sensitivity functions

$$F_{u_i} = K^a_{i0} + \sum_{j=1}^{n} K^a_{ij} \cos j\gamma + K^b_{ij} \sin j\gamma. \quad (6)$$

In the initial version of this work presented here, the intent is to show feasibility of the proposed output feedback methodology, hence a linearized control design which guarentees local asymptotic stability of speed regulation and obstacle avoidance responses will be discussed. Simulations of the full nonlinear dynamics and spatially discritized sensory system will be presented.

For analysis and simulation purposes we will use the dynamics of the hovercraft from the Caltech wireless testbed (Cremean *et al.*, 2002). The vehicle admits planar translational motion (surge, sway) and a single axis of rotary motion (yaw). In the inertial configuration (x, y, θ) the equations of motion $\dot{x} = f(x,u)$ are

$$\begin{aligned} m\ddot{x} &= (F_s + F_p)\cos\theta - b\dot{x} \\ m\ddot{y} &= (F_s + F_p)\sin\theta - b\dot{y} \\ J\ddot{\theta} &= (F_s - F_p)r_0 - c\dot{\theta}. \end{aligned} \quad (7)$$

The translational and rotational damping coefficients are denoted by b and c, respectively, the starboard and port thruster forces are denoted by F_s and F_p, and r_0 denotes the thruster moment arm. The vehicle mass is given by m and the rotational inertia about the yaw axis is J.

In the case of a planar tunnel, the goal of the control system will be to maintain a forward reference velocity and trajectory along the centerline $(\dot{x}, y, \dot{y}, \theta, \dot{\theta}) = (v_0, 0, 0, 0, 0)$, therefore it will be useful to introduce the following state and input definitions $v = \dot{x}$, $u_1 = F_s + F_p - bv_0$, and $u_2 = F_s - F_p$. Assuming small states (other than v) and control inputs, the linearized equations of motion for a centerline flight trajectory become

$$\begin{aligned} m\dot{v} &= u_1 + b(v_0 - v) \\ m\ddot{y} &= b(v_0\theta - \dot{y}) \\ J\ddot{\theta} &= r_0 u_2 - c\dot{\theta} \end{aligned} \quad (8)$$

Table 2 shows the sensory outputs a_0, a_1, b_1 and a_2 in inertial coordinates for this environment. The second column is the linearization $z(\boldsymbol{x}) = z(\boldsymbol{x}_0) + \sum_i \frac{\partial z}{\partial x_i}(\boldsymbol{x}_0)\ (x_i - x_{i0})$, with respect to the kinematic variables $\boldsymbol{x} = [\ v\ y\ \dot{y}\ \theta\ \dot{\theta}\ ]'$ along a reference trajectory $\boldsymbol{x}_0 = [\ v_0\ 0\ 0\ 0\ 0\ ]'$, corresponding to a centerline flight path at a constant velocity v_0. Notice in (8) that the v dynamics are decoupled from the y, θ dynamics and in Table 2 the linearized b_1 output is a function of v only and the linearized a_0, a_1, a_2

Table 2. Inertial WFI Sensory Outputs

WFI Sensory Output	Linearization $z(\boldsymbol{x})$
$a_0 = -\sqrt{2}\dot{\theta} + \frac{y}{\sqrt{2}(a^2-y^2)}\ v$	$-\sqrt{2}\dot{\theta} + \frac{v_0}{\sqrt{2}a^2}y$
$a_1 = \frac{4a}{3\pi(a^2-y^2)}\ (2v\sin\theta - \dot{y}\cos\theta)$	$\frac{4}{3\pi a}\ (2v_0\theta - \dot{y})$
$b_1 = \frac{4a}{3\pi(a^2-y^2)}\ (2v\cos\theta + \dot{y}\sin\theta)$	$\frac{8}{3\pi a}v$
$a_2 = -\frac{y}{2(a^2-y^2)}\ (v\cos 2\theta + \dot{y}\sin 2\theta)$	$-\frac{v_0}{2a^2}y$

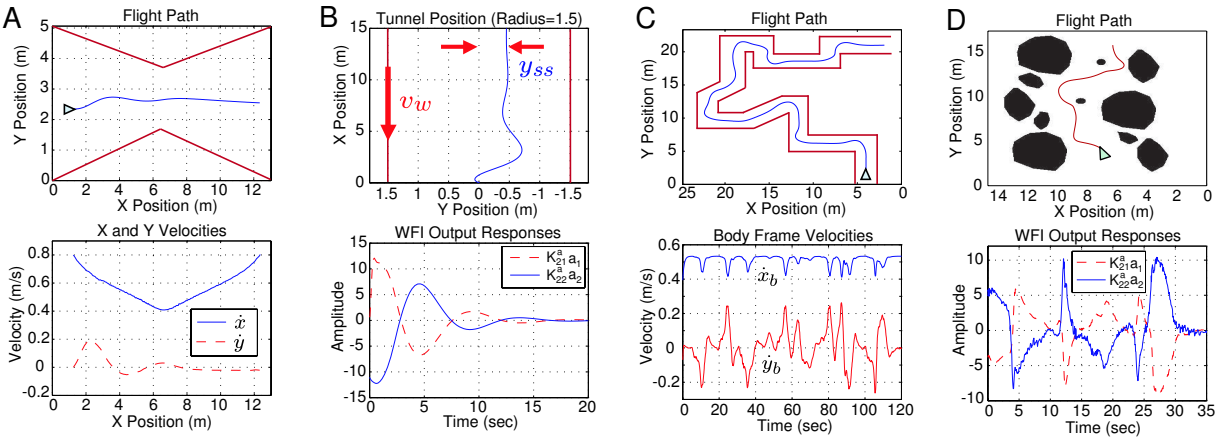

Fig. 5. Simulations of WFI-based navigation. (A) Clutter response for a converging-diverging tunnel (B) Centering response with a moving wall (C) Corridor navigation (D) Obstacle field navigation

outputs are functions of $y, \dot{y}, \theta, \dot{\theta}$. Hence, with the linearized system we can effectively decouple the control problem into the *clutter* (forward speed regulation) response and the *centering* (obstacle avoidance) response.

For the forward speed regulation task, we define a reference forward velocity r and corresponding scaling factor N and close the loop by setting the thrust input $u_1 = K^b_{11}(Nr - b_1)$, corresponding to the motion sensitivity function

$$F_{u_1}(\gamma) = K^b_{11} \sin\gamma. \tag{9}$$

With $r = v_0$, choose $N = 8/(3\pi a)$ for zero steady-state error, and the linearized closed loop dynamics become $\dot{v} = -\frac{1}{m}\left(K^b_{11}N + b\right)(v - v_0)$. One can easily verify that with $K^b_{11} > -b/N$ local stability is achieved.

For the underactuated hovercraft no control input is available in the sideslip (sway) direction. However, the lateral dynamics are coupled to the rotational dynamics through the $bv_0\theta$ term in (8), hence it is possible to accomplish stabilization of both flight modes through the torque input, taken to be $u_2 = K^a_{20}a_0 + K^a_{21}a_1 + K^a_{22}a_2$, corresponding to the motion sensitivity function

$$F_{u_2}(\gamma) = K^a_{20} + K^a_{21}\cos\gamma + K^a_{22}\cos 2\gamma. \tag{10}$$

The natural dynamics contain only inertial and viscous terms, therefore to achieve a stable centering/obstacle avoidance response, we require $K^a_{21} < 0$ for rotational stiffness and $K^a_{22} > 0$ for lateral stiffness. Additionally, rotational damping can be added with $K^a_{20} > 0$, however the linearization of the DC component a_0 of $\dot{Q}$ also has a lateral imbalance term (Table 2), hence we further need the restriction $K^a_{22} > \sqrt{2}K^a_{20}$ to provide the lateral stiffness required for a stable centering response. This can be verified by the characteristic equation for the linearized closed loop dynamics

$$\begin{aligned} &s^4 + \left(\frac{b}{m} + \frac{c + \sqrt{2}K^a_{20}}{J}\right)s^3 \\ &+ \left(\frac{bc}{mJ} + \frac{\sqrt{2}bK^a_{20}}{mJ} - \frac{4K^a_{21}v_0}{3\pi Ja}\right)s^2 \\ &- \frac{4K^a_{21}bv_0}{3\pi mJa}s + \frac{v_0^2 b(K^a_{22} - \sqrt{2}K^a_{20})}{2mJa^2} = 0. \end{aligned} \tag{11}$$

It is useful at this point to make some comparisons with experimental assays in tunnel navigation with honeybees, namely the converging-diverging tunnel and the moving wall (Srinivasan *et al.*, 1996). The converging-diverging tunnel investigated the clutter response, as it was observed bees regulated their forward flight speed in proportion to tunnel width; the more narrow the tunnel, the slower the flight speed. In the moving wall experiments, the centering response was examined. Honeybees were directed to fly down a tunnel with one of the walls moving at a constant rate along the flight path. It was observed that when the walls were stationary the bees tended to fly along the centerline, but when one wall was given constant motion along (against) the direction of travel, bees shifted their trajectories toward (away from) the moving wall.

We have constructed simulations based on the full nonlinear planar flight dynamics (7) to qualitatively compare the performance of the WFI control methodology to these experimental assays. Environments were defined as bitmaps, and the instantaneous optic flow was computed by estimating the depth at the current location and orientation at 60 equally-spaced circumferential points and combining it with the current kinematics according to (1). Force and torque control inputs are generated by taking the discrete inner product of the instantaneous optic flow with appropriately sampled versions of the motion sensitivity functions (9) and (10). Sensitivity gains K^a_{ij} and K^b_{ij} used in the simulation were chosen

based on the the performance index of maximizing the bandwidth of the slow (lateral) flight mode in the linearized closed loop system (11). Figure 5A shows the centering/clutter responses for the hovercraft navigating a converging-diverging tunnel; the forward speed is indeed proportional to tunnel width, as seen in (Srinivasan *et al.*, 1996).

Within the framework we have constructed we can investigate the moving wall assay by modifying the planar tunnel optic flow (1) with a constant left or right wall velocity bias $-v_w\ \hat{\boldsymbol{e}}_x = -v_w \cos\theta\ \hat{\boldsymbol{e}}_{x_b} + v_w \sin\theta\ \hat{\boldsymbol{e}}_{y_b}$. Hence, $\dot{x}_b \mapsto \dot{x}_b + v_w \cos\theta$ and $\dot{y}_b \mapsto \dot{y}_b + v_w \sin\theta$ for $0 \leq \gamma + \theta < \pi$ (left wall movement) or $\pi \leq \gamma + \theta < 2\pi$ (right wall movement). For left wall motion, the steady-state value $y = y_{ss}$ along the equilibrium trajectory $x_w : (v = v_0, y = y_{ss}, \dot{y} = 0, \theta = 0, \dot{\theta} = 0)$ that results in a zero torque input $u_2|_{x_w} = 0$ is $y_{ss} = -\frac{a v_w}{2v_0 + v_w}$. Motion opposite the flight direction ($v_w > 0$) will result in a shift right ($y_{ss} < 0$) of the steady-state flight path while motion along the flight direction ($v_w < 0$) will result in a shift left ($y_{ss} > 0$), as observed in (Srinivasan *et al.*, 1996). Also as $v_w \to 0$, $y_{ss} \to 0$ and as $v_w \to \pm\infty$, $y_{ss} \to \mp a$. The simulated hovercraft flight path for left wall motion with $v_w > 0$ is plotted in Figure 5B, along with the time response of the first two spatial cosine harmonics a_1,a_2 of the optic flow. As discussed in the previous section, a_2 provides a corrective torque for the lateral imbalance, and a_1 provides the opposing rotational stiffness required for stabilization.

The closed loop behavior of this output feedback methodology was also evaluated in more complicated environments. Using the same feedback structure and gains, the vehicle was directed to navigate a complicated corridor (Figure 5C) and an obstacle field (Figure 5D). Body velocities are shown for the corridor, and the response of the first two cosine harmonics of the optic flow are shown for the obstacle field.

4. CONCLUSIONS

A control-oriented analytical model for spatial wide-field integration (WFI) of retinal image flow was developed. The model provides a unique characterization of information available for feedback from WFI sensory systems, and establishes the connection between global structure of optic flow (retinal motion sensitivity patterns) and the control-relevant information available for feedback.

The analysis presented suggests a more general functional role for wide-field sensitive neurons in navigation and flight control as well as a novel methodology for utilizing optic flow in bio-inspired applications. Rather than implementing wide-field integrators as direct estimators of kinematics or depth, it was shown how the spatial harmonics of planar optic flow, extracted with motion-pattern sensitive kernels, correspond to feedback terms which can be used to stabilize various reflexive behaviors. The proposed WFI output feedback methodology is shown to be equivalent to stabilizing the closed loop dynamics with respect to spatial perturbations from a balanced nearness function, and has the advantage of being computationally inexpensive as each required control input can be computed with an inner product of vectors on the order of 60 elements.

Planar flight stabilization and navigation in complicated environments has been demonstrated in simulation, and it is shown that the proposed methodology has sufficient complexity to give rise to experimentally observed navigational heuristics as the centering and forward speed regulation responses exhibited by honeybees.

REFERENCES

Barrows, G.L., J.S. Chahl and M.V. Srinivasan (2003). Biologically inspired visual sensing and flight control. *The Aeronautical Journal* **107**, 159–168.

Borst, A. and J. Haag (2002). Neural networks in the cockpit of the fly. *J. Comp. Physiol. A* **188**, 419–437.

Cremean, Lars, William Dunbar, David van Gogh, Jason Hickey, Eric Klavins, Jason Meltzer and Richard M. Murray (2002). The caltech multi-vehicle wireless testbed. *Conf. on Decision and Control (CDC)*.

Egelhaaf, M. and A. Borst (1993). Motion computation and visual orientation in flies. *Comp. Biochem. Phisiol.* **104A**, 659–673.

Franz, M.O. and H.A. Mallot (2000). Biomimetic robot navigation. *Robotics and Autonomous Systems* **30**, 133–153.

Franz, M.O., J.S. Chahl and H.G. Krapp (2004). Insect-inspired estimation of egomotion. *Neural Computation* **16**, 2245–2260.

Frye, M.A. and M.H. Dickinson (2001). Fly flight: A model for the neural control of complex behavior. *Neuron* **32**, 385–388.

Gibson, J.J. (1950). *The perception of the visual world*. Houghton Mifflin. Boston.

Koenderink, J.J. and A.J. van Doorn (1997). Facts on optic flow. *Biol. Cybern.* **56**, 247–254.

Krapp, H.G., B. Hengstenberg and R. Hengstenberg (1998). Dendritic structure and receptive-field organization of optic flow processing interneurons in the fly. *J. Neurophysiol.* **79**, 1902–1917.

Srinivasan, M.V., S.W. Zhang, M. Lehrer and T.S. Collet (1996). Honeybee navigation *en route* to the goal: visual flight control and odometry. *J. Exp. Biol.* **199**, 237–244.